

THE MATRYOSKA RUN (II): TIME DEPENDENT TURBULENCE STATISTICS, STOCHASTIC PARTICLE ACCELERATION AND MICROPHYSICS IMPACT IN A MASSIVE GALAXY CLUSTER

FRANCESCO MINIATI

Physics Department, Wolfgang-Pauli-Strasse 27, ETH-Zürich, CH-8093, Zürich, Switzerland; fm@phys.ethz.ch
Draft version September 22, 2018

ABSTRACT

We use the Matryoshka run to study the time dependent statistics of structure-formation driven turbulence in the intracluster medium of a $10^{15} M_{\odot}$ galaxy cluster. We investigate the turbulent cascade in the inner Mpc for both compressional and incompressible velocity components. The flow maintains approximate conditions of fully developed turbulence, with departures thereof settling in about an eddy-turnover-time. Turbulent velocity dispersion remains above 700 km s^{-1} even at low mass accretion rate, with the fraction of compressional energy between 10% and 40%. Normalisation and slope of compressional turbulence is susceptible to large variations on short time scales, unlike the incompressible counterpart. A major merger occurs around redshift $z \simeq 0$ and is accompanied by a long period of enhanced turbulence, ascribed to temporal clustering of mass accretion related to spatial clustering of matter. We test models of stochastic acceleration by compressional modes for the origin of diffuse radio emission in galaxy clusters. The turbulence simulation model constrains an important unknown of this complex problem and brings forth its dependence on the elusive micro-physics of the intracluster plasma. In particular, the specifics of the plasma collisionality and the dissipation physics of weak shocks affect the cascade of compressional modes with strong impact on the acceleration rates. In this context radio halos emerge as complex phenomena in which a hierarchy of processes acting on progressively smaller scales are at work. Stochastic acceleration by compressional modes implies statistical correlation of radio power and spectral index with merging cores distance, both testable in principle with radio surveys.

Subject headings: acceleration of particles – galaxies: cluster: intracluster medium – large-scale structure of Universe – turbulence – methods: numerical – radiation mechanisms: non-thermal

1. INTRODUCTION

Astrophysical flows are well known to be turbulent for the most part. However, with due exceptions (Porter & Woodward 2000; Viallet et al. 2013; Bodo et al. 2011; Parkin & Bicknell 2013), this character of the flow is generally not reproduced in numerical models. The reason is simply due to the impractical computational cost. Turbulence requires the resolution of a large range of spatial scales, because it does not develop unless the flow's Reynolds number Re is sufficiently large. Nevertheless, there has been growing attention to the role of turbulence in recent years, calling for renewed efforts in achieving high Re flows in numerical models. This is particularly the case of the intra-cluster medium (ICM), the hot and magnetised plasma pervading the volume of galaxy clusters (GC).

In the ICM, as in other like flows, turbulence regulates the magnetic field energy density and structure (Subramanian et al. 2006; Iapichino & Niemeyer 2008). Knowledge of the statistical properties of the turbulence and of its time evolution is essential to evaluate fundamental quantities such as the equipartition scale between magnetic and kinetic energy (Ryu et al. 2008; Cho et al. 2009; Beresnyak 2012). Also, turbulence acts as an effective non-thermal pressure supporting the ICM gas against self-gravity (Faltenbacher et al. 2005; Dolag et al. 2005; Nagai et al. 2007; Lau et al. 2009; Biffi et al. 2011; Valdarnini 2011). This induces a bias in the mass estimates of GC which propagates as a systematic error when such estimates are employed in cosmology. Again,

proper resolution of the turbulent flow is important to estimate the turbulent energy density across the relevant scales and accurately determine the above biases (Miniati 2014). Finally, cluster turbulence influences the transport of relativistic particles both in coordinate and momentum space. In fact, a significant fraction of GC betray the presence of giant halos of diffuse radio emission extending over distances \sim Mpc (Ferrari et al. 2008; Ferretti et al. 2012; Brunetti & Jones 2014). The nature of this phenomenon is unknown but, upon inspection, it reveals that relativistic electrons must be accelerated in the ICM (Jaffe 1977). In addition, the phenomenon appears to be triggered by major merger events (Buote 2001; Ferrari et al. 2003; Clarke & Enßlin 2006; Cassano et al. 2010b, see also Russell et al. (2011); Basu (2012)). Amongst other proposals (Blasi & Colafrancesco 1999; Miniati et al. 2001a; Keshet & Loeb 2010; Pfrommer et al. 2008; Enßlin et al. 2011) a compelling and popular idea for the origin of radio halos (RH) is that the relativistic particles responsible for the radio emission are accelerated by turbulence (e.g. Schlickeiser et al. 1987) particularly when generated in connection with a major merger event (e.g. Brunetti et al. 2001; Petrosian 2001). In particular, in recent years, much effort has been devoted to models based on compressional turbulence (Brunetti & Lazarian 2007, 2011, referred to in the following as BL7 and BL11, respectively).

Several numerical studies have already addressed such connection between merger driven turbulence and the origin of RH (e.g. Vazza et al. 2009; Paul et al. 2011;

Vazza et al. 2011; Hallman & Jeltema 2011; Beresnyak et al. 2013; Donnert et al. 2013; Donnert & Brunetti 2014). In particular Beresnyak et al. (2013) employed a sophisticated spectral decomposition scheme to estimate the acceleration rates from compressible modes using results from an MHD-AMR cosmological simulation of a galaxy cluster. In their analysis they focus on an individual time frame, hence the time evolution is not explored, and study in detail the role of the cosmic-ray feedback on the turbulence. In addition, Donnert et al. (2013) and ZuHone et al. (2013) have carefully followed the stochastic acceleration of relativistic particles during merger and sloshing motions, respectively, using more approximate turbulence, mode decomposition and cluster models in their non-cosmological simulations. A numerical model is useful in that it provides an estimate of the turbulent energy in the ICM. This quantity impacts the transport coefficients, hence the acceleration rates of particle. In the aforementioned acceleration models, it is the compressional component of the turbulent motion that interacts with, and supplies energy to, the relativistic particles. In addition, the calculation of the acceleration rates requires knowledge of other characteristics of the turbulence cascade, namely the outer scale, velocity dispersion and slope. In order to determine these quantities, the numerical model must resolve the turbulence cascade. In addition, these quantities should ideally be determined as a function of time during the GC's formation history. It is, in fact, the rise of turbulent energy, following a major merger that is believed to power RH. Thus it is important to determine how the turbulent cascade changes in normalisation and slope in response to the changing conditions of mass accretion rate and merger events. This important aspect of the problem remains to be studied and is the objective of this paper.

Indeed, thanks to advances in computational techniques and supercomputer power we have recently been able to model the statistical properties of ICM turbulence in a fully cosmological context (Miniati 2014). The focus of the calculation is the formation and evolution of a massive GC with virial mass, $M = 1.3 \times 10^{15} M_{\odot}$ at redshift, $z = 0$. This system is particularly interesting from the viewpoint of the origin of RH, because it undergoes a major merger around $z = 0$. In the first paper (Miniati 2014) we have introduced the methodology adopted in carrying out the numerical calculation, and presented the statistical analysis of the ICM turbulence for a single time snapshot corresponding to $z \simeq 0$.

In this paper we study, instead, the time evolution of the statistical properties of the ICM turbulence. In doing so we give priority to those properties most relevant to the acceleration of particles. In fact, in the second part of the paper we use our findings on the ICM turbulence to explore their implications in terms of particle acceleration and, possibly, on the origin of RH. We explore in particular two acceleration models, the non-resonant mechanism (NR, Ptuskin 1988) and transient-time-damping (TTD, Fisk 1976; Miller 1991), both advocated and studied in great details for the ICM case in BL7 and BL11. As already anticipated, both processes are powered by the compressional component of the turbulence. However, additional physics of the ICM plasma is at work here, which is not completely established and which is not directly modelled by the numerical simula-

tion. We have therefore explored different assumptions about such physics and found that they have important consequences on the results. In fact, one of the great advantages and most valuable contribution of a high resolution numerical model such as this, is that by resolving the turbulence cascade of compressional and incompressible motions it narrows an important unknown of this complex problem, and brings forth the implications of other assumptions concerning the elusive and difficult to test micro-physics of the ICM plasma.

The remainder of this paper is organised as follows. In Section 2 we introduce the methods employed in the paper, including the details of the numerical simulation (2.1) and the analysis to extract the turbulent statistics (2.2). In Section 3 we present the results concerning the time-evolution of the GC: this includes the mass accretion history, the evolution of the turbulent kinetic energy and the fraction in compressional motions thereof (3.1); as well as the evolution of the turbulence statistics such as second order structure functions, slope of the cascade inertial range, pdf of the velocity increments at the turbulence outer scale (3.2). Section 4 presents the second part of results, those concerning the acceleration of particles. In particular we introduce the diffusion coefficients (4.1) and cascade models (4.2) used in estimating the particle advection rates in momentum space and discussing their implications in connection with the origin of RH (4.3). We discuss the results in Section 5 and conclude with a summary and conclusions in Section 6.

2. METHODS

2.1. Numerics

The Matryoshka run, including the novel Eulerian refinement approach, is fully described in Miniati (2014). The run is carried out with CHARM an Adaptive-Mesh-Refinement code for cosmology, based on a directionally unsplit variant of the Piecewise-Parabolic-Method for hydrodynamics (Colella 1990), a time centered modified symplectic scheme for the collisionless dark matter and solve Poisson's equation with a second order accurate discretization (Miniati & Colella 2007). We also evolve a dynamically negligible magnetic field using the constrained-transport algorithm for solenoidal MHD described in Miniati & Martin (2011). Radiative cooling and heating are neglected. The cosmological model corresponds to a concordance Λ -CDM universe with normalized (in units of the critical value) total mass density, $\Omega_m = 0.2792$, baryonic mass density, $\Omega_b = 0.0462$, vacuum energy density, $\Omega_{\Lambda} = 1 - \Omega_m = 0.7208$, normalized Hubble constant $h \equiv H_0/100 \text{ km s}^{-1} \text{ Mpc}^{-1} = 0.701$, spectral index of primordial perturbation, $n_s = 0.96$, and rms linear density fluctuation within a sphere with a comoving radius of $8 h^{-1} \text{ Mpc}$, $\sigma_8 = 0.817$ (Komatsu et al. 2009). The computational volume comoving size is $L_{Box} = 240 h^{-1} \text{ Mpc}$. Here the baryonic and dark matter variables are initialised with `grafic++` (a parallel version of `grafic2` (Bertschinger 2001), made publicly available by D. Potter) using the power spectrum interpolation method suggested in Eisenstein & Hu (1998).

The purpose of the simulation is to model at high resolution the formation of a massive GC. The latter was identified in a preliminary low resolution run at redshift zero with our implementation of the HOP halo

finder (Eisenstein & Hut 1998) Thus we generate zoom-in type of initial conditions, on three progressively finer and uniform resolution grids. The coarsest level grid is made of 512^3 comoving cells, corresponding to a nominal spatial resolution of $468.75 h^{-1}$ comoving kpc, and the collisionless dark matter component is represented with 512^3 particles of mass $6.7 \times 10^9 h^{-1} M_\odot$. A region of space surrounding the Lagrangian volume of the target GC, is then initialised at higher resolution with the help of two additional levels of refinement on top of the base grid. The refinement ratio for both levels is, $n_{\text{ref}}^\ell \equiv \Delta x_\ell / \Delta x_{\ell+1} = 2$, $\ell = 0, 1$. Each refined level covers 1/8 of the volume of the next coarser level with a uniform grid of 512^3 comoving cells while the dark matter distribution function is represented by 512^3 particles. At the finest level the spatial resolution is $\Delta x = 117.2 h^{-1}$ comoving kpc and the particle mass is $1.0 \times 10^8 h^{-1} M_\odot$. In addition, as the Lagrangian volume of the GC shrinks under self-gravity, three additional uniform grids covering 1/8 of the volume of the next coarser level with 512^3 , 1024^3 and 1024^3 comoving cells are employed, with a corresponding refinement ratio $n_{\text{ref}}^\ell = 2, 4, 2$, for $\ell = 2, 3, 4$, respectively. All of these additional three grids are in place by redshift 1.4, providing a spatial resolution of $7.3 h^{-1}$ comoving kpc in a volume of $7.5 h^{-1}$ Mpc, which accommodates the whole virial volume of the GC. The ensuing dynamic range of resolved spatial scales is sufficiently large for the emergence of turbulence.

2.2. Analysis of Turbulence Velocity Field

The exquisite resolution across the GC volume allows us to accurately measure the time dependent statistical properties of the turbulent motions. In particular we compute the longitudinal and transverse second order structure functions for both the solenoidal and compressional components of the velocity. To do so we first carry out the following Hodge-Helmholtz decompositions,

$$\mathbf{v} = \mathbf{v}_s + \mathbf{v}_c, \quad (1)$$

$$\mathbf{v}_c = -\nabla\phi, \quad \mathbf{v}_s = \nabla \times \mathbf{A}, \quad (2)$$

$$\phi = \frac{1}{4\pi} \int \frac{\nabla \cdot \mathbf{v}}{r} d\mathbf{x}, \quad \mathbf{A} = \frac{1}{4\pi} \int \frac{\nabla \times \mathbf{v}}{r} d\mathbf{x}. \quad (3)$$

Then, for each component we can define the second order rank correlation function of velocity increments (Landau & Lifshitz 1987)

$$S_{ij}(\mathbf{x}, \boldsymbol{\ell}) \equiv \langle \delta v_i \delta v_j \rangle, \quad (4)$$

where i indicates the vector component along i -th axis and $\delta v_i \equiv [\mathbf{v}(\mathbf{x} + \boldsymbol{\ell}) - \mathbf{v}(\mathbf{x})]_i$. For a homogeneous and isotropic flow this tensor is only a function of $\ell = |\boldsymbol{\ell}|$ and can be expressed in terms of the longitudinal and transverse correlation functions (Landau & Lifshitz 1987),

$$S_{ij}(\ell) = S_l^{(2)}(\ell) n_i n_j + S_t^{(2)}(\ell) (\delta_{ij} - n_i n_j) \quad (5)$$

where $S_l^{(2)}$ and $S_t^{(2)}$ are computed by taking in Eq. 4 the velocity components parallel and perpendicular to $\boldsymbol{\ell}$, respectively. For isotropic and homogeneous turbulence one can also write (Landau & Lifshitz 1987)

$$S_{ij}(\ell) = \frac{2}{3} \langle (\delta \mathbf{v})^2 \rangle \delta_{ij} - 2s_{ij}(\ell) \quad (6)$$

where $s_{ij}(\ell) = \langle [\mathbf{v}(\mathbf{x})]_i [\mathbf{v}(\mathbf{x} + \boldsymbol{\ell})]_j \rangle$. Since the velocity components become uncorrelated at large distances, the asymptotic behaviour is as follows

$$\lim_{\ell \rightarrow \infty} s_{ij} = 0, \quad \lim_{\ell \rightarrow \infty} S_{ij} = \frac{2}{3} \langle (\delta \mathbf{v})^2 \rangle \delta_{ij}. \quad (7)$$

The asymptotic behaviour of S_{ij} can be reliably computed from the numerical simulations, which allows to also accurately infer s_{ij} . The total second order velocity correlation function is then given by

$$s^{(2)}(\ell) = s_\ell^{(2)}(\ell) + 2s_t^{(2)}(\ell). \quad (8)$$

The correlation functions in configuration space can be converted into a power spectrum of isotropic velocity fluctuations through a Fourier transformation, namely,

$$s^{(2)}(k) = \int_0^\infty d^3r s^{(2)}(r) e^{-i\mathbf{k} \cdot \mathbf{r}} = s_0 \left(\frac{k}{k_L} \right)^{-\zeta_2 - 3}, \quad (9)$$

where the last equality applies to the inertial range, k_L is the mode corresponding to the largest scale and ζ_2 , the slope of the second order structure function. The integral can be carried through to determine s_0 from the normalisation of $s(\ell)$

$$\langle (\delta \mathbf{v})^2 \rangle = \int dk 4\pi k^2 s^{(2)}(k), \quad (10)$$

so that

$$s_0 = \frac{\zeta_2 \langle (\delta \mathbf{v})^2 \rangle}{4\pi k_L^3}. \quad (11)$$

Note that with the above notation the kinetic energy spectrum is

$$E(k) = \zeta_2 \frac{\langle (\delta \mathbf{v})^2 \rangle}{2k_L} \left(\frac{k}{k_L} \right)^{-\zeta_2 - 1}. \quad (12)$$

In addition, in the following certain quantities are computed in terms of the total energy spectrum, $W(k)$, which includes in addition to the kinetic component also the potential component associated to pressure fluctuations. To good approximation the two are in equipartition (e.g. Sarkar et al. 1991), which will be assumed here (see also BL7), i.e.

$$W(k) \approx 2E(k). \quad (13)$$

To compute the structure function we define sampling points randomly distributed inside the volume of interest and compute the velocity difference with respect to randomly selected field points at a maximum distances of two virial radii. A total of 10^6 sampling points and 10^6 field points are used for this purpose for a total of 10^{12} pairwise velocity increments. In our analysis we do not attempt to filter out large scale uniform motions explicitly (see, e.g. Vazza et al. 2011). The structure functions are actually designed to do that and $S(\ell)$ does not include contributions from flows that are coherent above the scale, ℓ . A comparison with other methods in the literature is beyond the scope of the paper. However, it is worth noting that our results, presented in Section 3.2, indicate that the scales at which the structure functions flatten, which we identify with the turbulence outer scale, are consistent with the results in, e.g., Vazza et al. (2011),

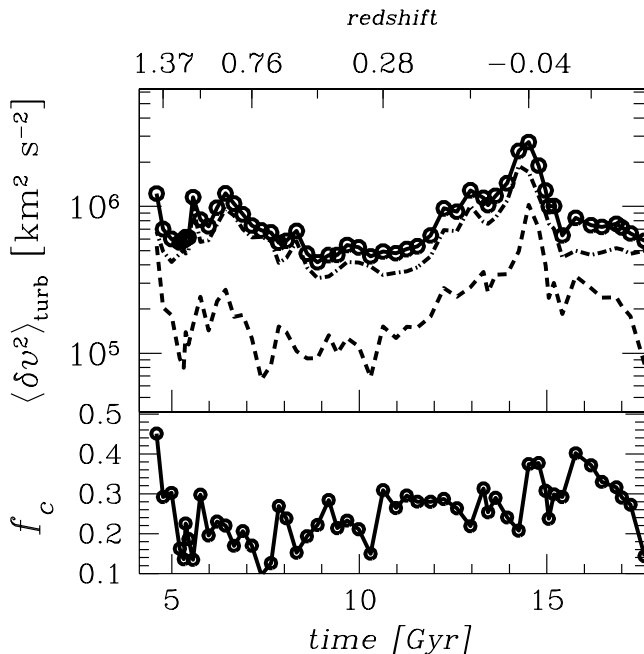


Figure 1. *Top:* Time evolution of the turbulent velocity dispersion. The incompressible and compressional components are represented with a dot-dashed and dashed line, respectively, and their sum with a solid line and open dot symbols. *Bottom:* Fraction of turbulent velocity dispersion in the compressional component.

who use a low-pass filter (the k-max method) to remove what they considered large scale motions unrelated to turbulence. In the following we restrict the analysis of the velocity field, including the velocity structure functions, to the region within 1 Mpc from the GC centre. This is the most interesting region from the point of view of astronomical observations. In particular, the diffuse radio-halo emission is observed primarily within this limited volume and in the final part of the paper we attempt to apply our findings concerning the properties of turbulence to models of particle acceleration by compressional motions.

Note, that the statistics of turbulence can also be characterised in terms of power spectra obtained through an analysis in Fourier space. This analysis is in principle equivalent since power spectra and structure functions are related through a Fourier transformation. Fourier analysis is less expensive (scaling with the number of points N as $N \times \log(N)$), hence in principle preferable, but it requires periodic boundary conditions which in the case of a cluster have to be constructed artificially. Structure functions are more expensive (scaling instead as N^2) but do not require a choice of boundary conditions, proving particularly useful to compute the turbulence statistics in a selected region of the galaxy cluster volume (like in a thick shell).

3. RESULTS (I): HYDRODYNAMIC TURBULENCE

3.1. Accretion History

The mass accretion history of this system is mildly irregular, due to the alternate dominance of substructure infall and smooth accretion, but remains quite uneventful until $z \approx 0.3$. After this time the accretion rate increases significantly, culminating with two mergers events, a minor and a major one. The accretion history is reflected

in the level of turbulent energy that is present in the ICM. The turbulent velocity dispersion (see Eq. 10) is reported as a function of time and redshift in Fig. 1. The solid line with open circles in the top panel correspond to the total velocity field, while the dot-dashed and dashed lines correspond to the incompressible and compressional components, respectively. Their ratio as a function of time is reported in the bottom panel of the same Figure. At the earliest times in the Figure, $z \approx 1$, the turbulent velocity oscillates between several 10^2 and a 10^3 km s^{-1} . It then settles at several hundred km s^{-1} between $0.8 \gtrsim z \gtrsim 0.14$. This is a apparently a time of relatively low mass accretion rate. Nevertheless, the drop in turbulent energy is modest, indicating that turbulence is generated efficiently by mass accretion. This is not surprising with hindsight given that the dissipation of kinetic energy associated with accretion is very inefficient (Miniati 2014; Miniati et al. 2000). Finally, at $z \gtrsim 0.14$ the turbulent energy begins to ramp up. It peaks at $z \approx -0.4$ after reaching a secondary peak at $z \approx 0.05$. The increase in turbulent energy is associated with two merger events, a minor one followed by a major one, described below in further details. In particular, the two peaks in the Figure correspond to the time of core passage. Note that between $z \approx 0.3$ and $z \approx -0.4$ the turbulent energy has increased by a factor six. The bottom panel of Figure 1 shows the fraction of turbulent energy in the compressional component. This ratio is always smaller than one and oscillates between 10% and 40%. There appears to be a correspondence between the higher values of this ratio and the higher values of the turbulent energy (top panel). In particular, this ratio increases during the two merger events.

The interval in which the mass accretion and turbulent energy are particularly high lies between $0.15 \gtrsim z \gtrsim -0.06$. Figure 2 shows the evolution of the merger during this specific period of time. Each panel contains the density distribution in log scale on a plane passing approximately through the GC centre. Time, shown in the top-left corner of each panel, increases from top-left to bottom-right. In the first panel (top-left) the main GC is visible at the centre, and is surrounded by a large structure to the left and two smaller structures, one to the top-right of (SubA), and the other below (SubB), the main GC. The latter structure is actually not so visible because its centre lies on a slightly offset plane. The first merger experienced by the GC is due to the accretion of the two substructures, SubA and SubB. Since the substructure SubA is larger than SubB and its mass ratio to the GC is only 1/10, we are dealing with is a minor merger. It turns out, however, that SubA and SubB arrive at the GC core simultaneously and collide against each other (see top-centre and top-right panels). Despite the minor merger substantial turbulence is stirred up in the ICM. The minor merger culminates at 12.9 Gyr (middle-left panel). Half a billion yr later the second merger takes place. In this case the mass ratio is 1/2.5, so this corresponds to a major merger event. The merger is in full swing by 13.9 Gyr (middle right panel) and core passage, i.e. crossover of the merging GC cores, occurs around 14.2 Gyr (bottom left panel). After that, the merging system expands inertially and the turbulence decays rapidly.

Using a standard approach (Benson 2005; Wetzel 2011;

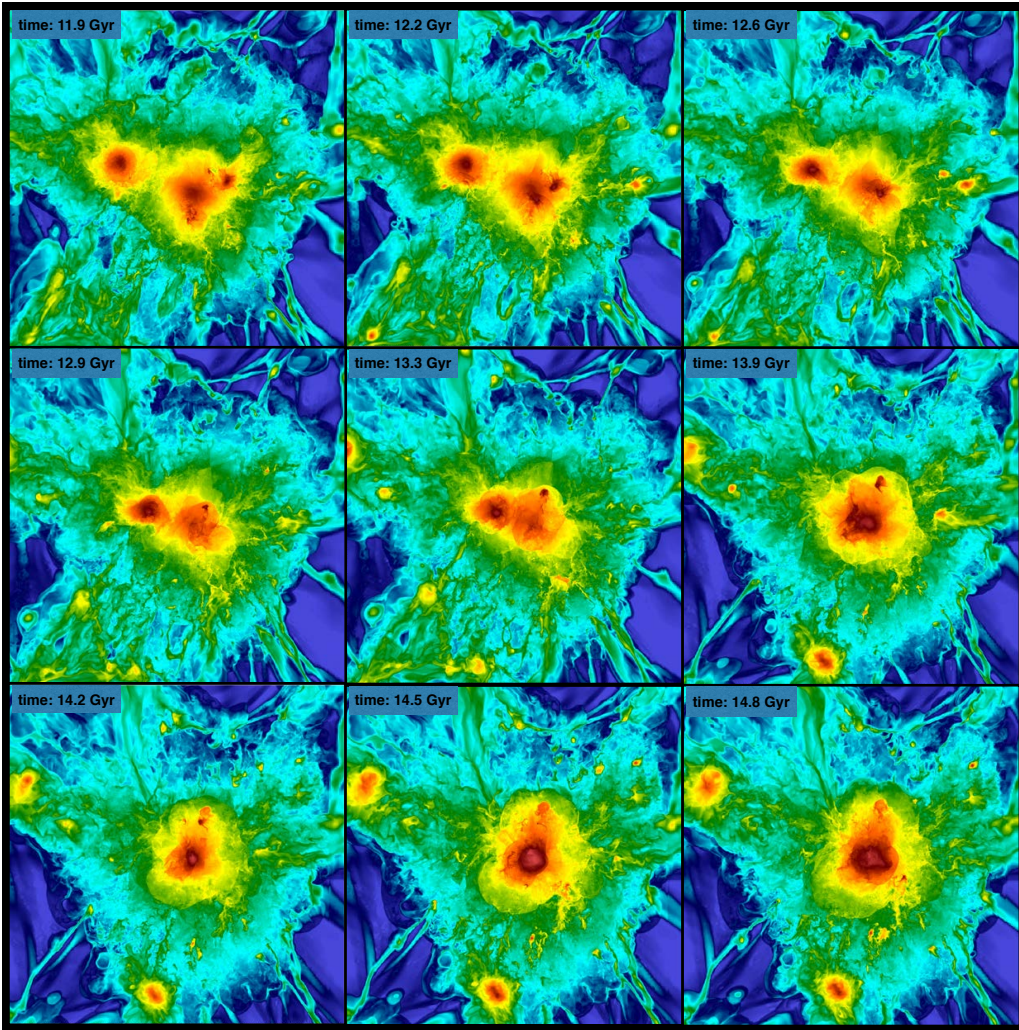


Figure 2. Merger history during the redshift interval $0.15 \lesssim z \lesssim -0.06$. Each panel shows the density distribution in log scale on a plane passing approximately through the GC centre. Time (in the top-left of each panel) increases from top-left to bottom-right. The top-left panel shows the main GC at the centre, a large substructure on the left with mass ratio 1:2.5 and two smaller substructures: the largest with mass ratio 1:10 to the top-right (SubA) of the main GC and the other (SubB) below it. The first merger experienced by the GC is due to the accretion of these two structures and culminates at $t=12.9$ billion yr (middle-left panel). The second merger with the largest substructure is in full swing by $t=13.9$ billion yr (middle right), with core passage around $t=14.2$ billion yr (bottom left).

Lee & Komatsu 2010) for the major merger case we have also estimated the infall radial velocity of the substructure when located at the virial radius of the main GC. This velocity is 1642 km s^{-1} , to be compared to a virial velocity of 1024 km s^{-1} . Thus this merger is quite energetic as such a high ratio of radial to virial velocity occurs only in less than 5% of mergers according to the statistical analysis of Benson (2005)

It is interesting to note that the turbulent energy remains sustained for $\gtrsim 3$ Gyr, i.e. much longer than the duration of the major merger of $\simeq 1$ Gyr. From the rapid decrease following its main peak (at $z \approx -0.4$) it is clear that the sustained regime of turbulent energy is not due to sloshing following the first core passage. Rather, the turbulent energy remains high for an extended period of time because the major merger is not an isolated accretion event. Prior to that, a minor merger has occurred as already mentioned and several other smaller substructures happened to accrete at that time. This fact is not occasional, but reflects the clustered character of matter distribution in the large scale structure of

the universe. So rare events of major merger activity are likely accompanied by additional mergers of smaller structures, causing relatively high level of turbulence beyond the short duration of the major merger itself. This point can only emerge when one studies the full time evolution of the turbulence in a cosmological setting and can thus compare the level of turbulence during relaxed and unrelaxed conditions. In addition, it the details of mass accretion might be important when making the connection between mergers and diffuse radio emission, because a triple merger of even two minor substructure can rise significant of turbulence.

3.2. Time Dependent Statistics

In this Section we discuss the evolution of the statistical properties of the turbulence focusing on the time interval $0.28 \lesssim z \lesssim -0.09$, which encompasses both the extended period of high turbulent energy and the time prior to it when the turbulence level was at a minimum.

We begin with second order structure functions shown at different times in Figure 3, for both the incompressible

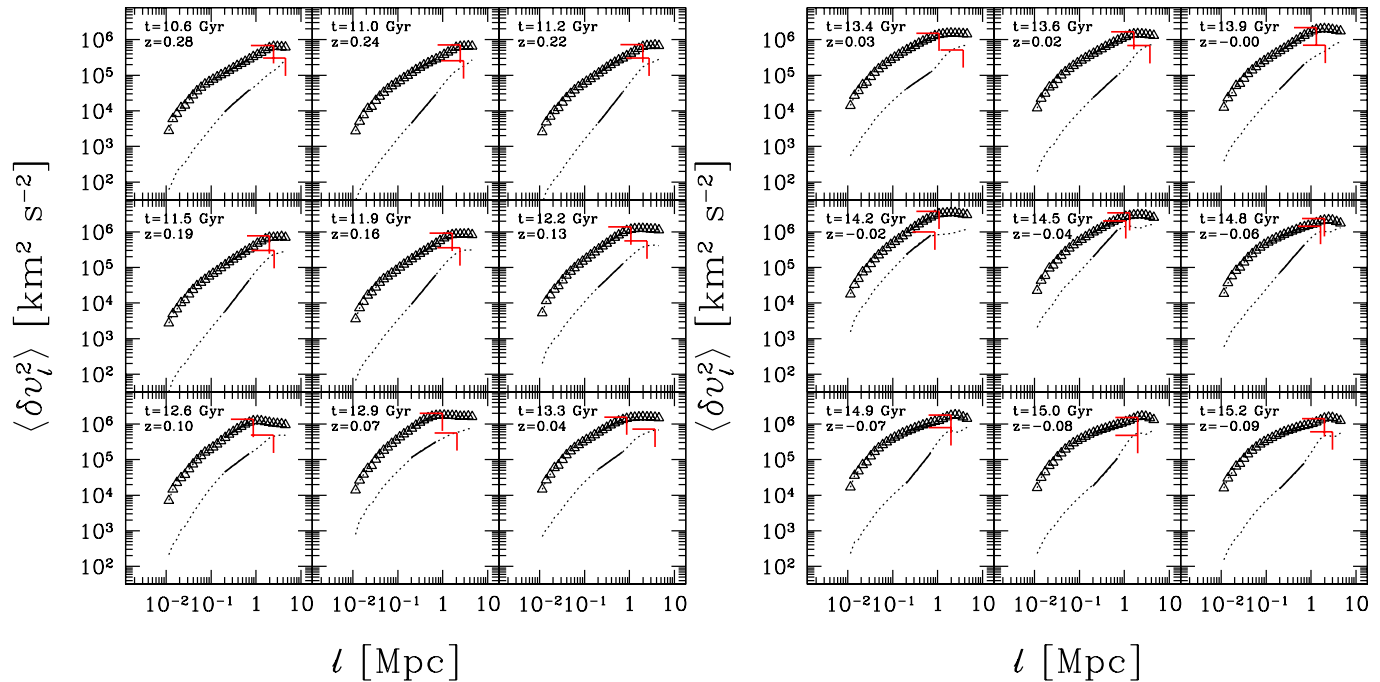


Figure 3. Total second order velocity structure functions (see Eq. 8) for solenoidal (triangles) and compressional (dots) components, respectively. For each component, the solid line represents the normalisation and slope in the inertial range extracted by our fitting procedure, while the vertical and horizontal red line the injection scale and the corresponding velocity increment. Time and redshift are indicated in the top left corner of each panel.

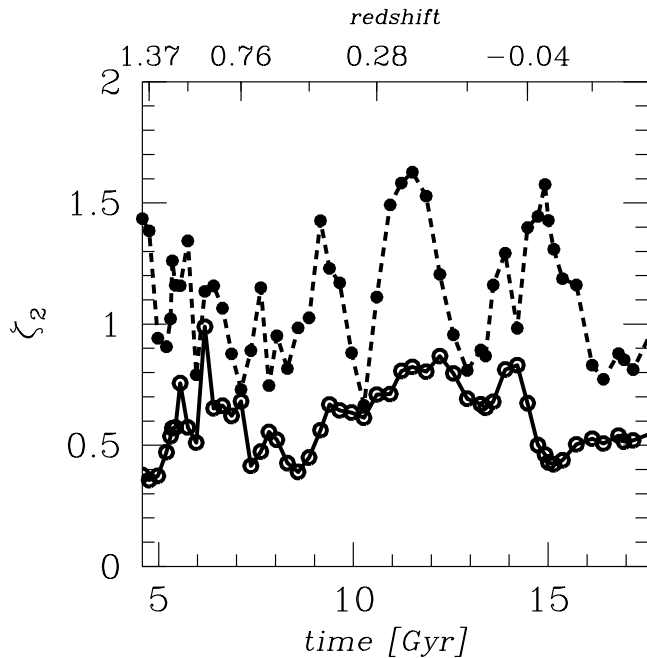


Figure 4. Slope of the structure functions' inertial range as a function of time for both the incompressible (solid line and open symbols) and compressional (dashed line and solid symbol) velocity components.

(triangles) and compressional (dots) velocity component. The structure functions are computed within a region of one Mpc from the GC centre (see 2.2). The numerical aspects concerning the modelling of turbulence in structure formation simulations are fully discussed in Miniati (2014, and references therein). In general the high resolution allows us to resolve at least one decade of scales in the inertial range of the turbulent cascade: from the

injection scale, typically a Mpc, to the scales affected by numerical viscosity, roughly 32 resolution element, i.e. 0.1 comoving Mpc.

We have thus identify the inertial range of the structure functions and computed the corresponding slope and normalisation. These are represented by the solid lines superposed to the triangles and dots. Based on the flattening of the structure functions, we have then identified for each velocity components the injection scale, L (red *vertical* solid lines in Figure 3). By extrapolating the velocity from the inertial range to L , we finally obtain the asymptotic velocity increment (red *horizontal* solid lines in Figure 3). Figure 3 shows that it is fairly straightforward to identify such quantities. In particular the inertial range is rather well defined. Occasionally, however, the inertial range of the structure functions of the compressional component appears as a broken power law, indicating departure from steady state conditions. In this case, our extrapolation procedure leads to velocity estimates slightly offset from the dotted curve itself. This is unavoidable consequence of our simplified representation of the structure functions with few parameters, in the case of departure from simple power-law. The theory/models to which this results will be applied in Sec. 4 do not warrant the use of additional parameters on the basis of accuracy, therefore we will tolerate the inaccuracy. In fact, these issues arises primarily during pre and post-merger phases, not during the crucial stages of the merger itself (around core passage), so it does not affect the results discussed in Section 4. In any case our estimates remain conservative and, if anything, overestimate the turbulent kinetic energy. Finally note that, while it would be possible to evaluate the outer scale and velocity independently of the inertial range, we think this would be even less representative of the turbulent cascade.

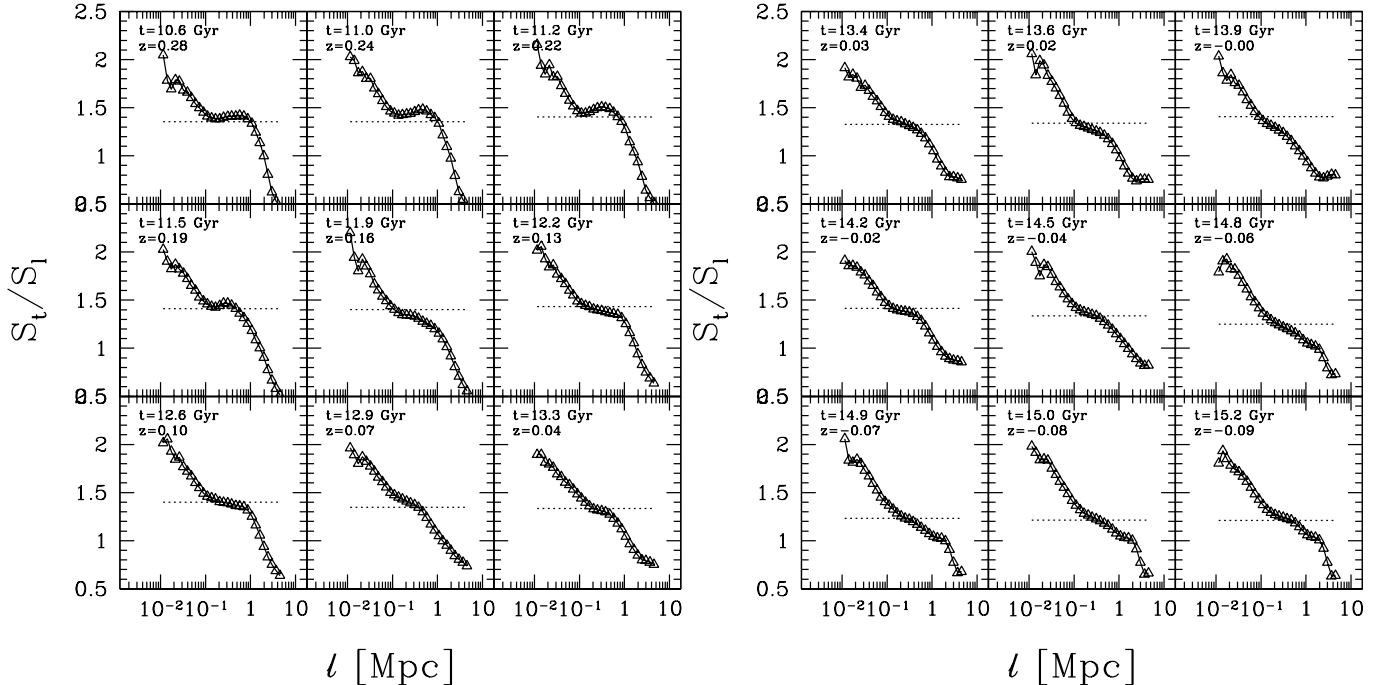


Figure 5. Ratio of transverse to longitudinal structure functions for the incompressible velocity component as measured from the simulation velocity data (triangle) versus expected value within the inertial range for fully-developed, steady-state, isotropic and homogeneous turbulence (dots).

According to Figure 3 the structure functions change both in normalisation and slope as a function of time. This happens in response to the changing mass accretion rate and merger events, which obviously changes the level of turbulent energy in the ICM. Figure 4 shows in detail the time dependence of the structure functions' slopes in the inertial range. The structure function is always steeper for the compressional than for the incompressible velocity. In addition its changes are considerably larger and on shorter timescales. After $t=10.6$ Gyr the turbulence starts to settle to a low level (see Sec. 3.1). Both structure functions steepen. The slopes tend to 0.8 and 1.5 for the incompressible and compressible components, respectively (see Figure 4). After $t=12$ Gyr the minor merger discussed above begins to take place and both structure functions become progressively flatter and with a larger normalisation. Their slopes become comparable at the peak of the merger, although the compressional component remains always steeper. During the short time separating the first (minor) and second (major) merger, the compressional turbulence decays quickly, its structure function steepens and breaks, in contrast to the slow evolution of the incompressible counterpart. The decay of the turbulence is interrupted by the occurrence of the second merger. For both components, the normalisation increases again while the slope flattens. The two structure functions at $t=14.2$ Gyr are almost parallel. After core passage the compressional turbulence again decays rather quickly, helped by the re-expansion of the ICM driven by the departing motions of the merging structures. In contrast, the incompressible component decays very slowly while its spectrum appears to get flatter, as if receiving additional power at intermediate scales.

In Figure 5 we plot as a function of spatial separation and for the same time sequence as Figure 3, the ratio

of the transverse to longitudinal second order structure functions of the incompressible velocity component. For fully developed, incompressible, isotropic and homogeneous turbulence, in the inertial range of the structure functions this ratio is expected to be (de Kármán & Howarth 1938; Landau & Lifshitz 1987),

$$\frac{S_{s,t}^{(2)}}{S_{s,l}^{(2)}} = 1 + \frac{1}{2}\zeta_2. \quad (14)$$

The predicted value is also plotted as a dotted line in each panel of Figure 5, according to the time dependent slope of the structure functions. Note that the dissipative effect of numerical viscosity appears below 0.1 Mpc and is strongly anisotropic, i.e. it preferentially damps the longitudinal velocity increments (Miniati 2014). In any case, the conditions for fully developed turbulence appear to be approximately fulfilled above the numerical dissipation scale and below the injection scale \sim Mpc. This is sufficient to warrant our approach based on the evaluation of the total structure functions in Eq. 8. While the quality of such fulfilment is obviously not perfect, this is not a numerical artefact but due to the nature of the ICM. Interestingly, departures from steady-state conditions appear to be worse at times when the turbulence is weak, $z \gtrsim 0.2$ and $z \lesssim -0.06$, and immediately before core passage, $t = 12.9$ and $t = 13.9$.

Finally, in Figure 6 we present the cumulative distribution function of the velocity increment for a separation scale corresponding to the injection scale (where the velocity increments are largest). The left and right panels are for the compressional and solenoidal velocity components, respectively. The dashed (red) vertical line marks the median value of the velocity whereas the solid (blue) vertical line the 12.5th percentile. Time in the left and right panels is the same as in the corresponding panels

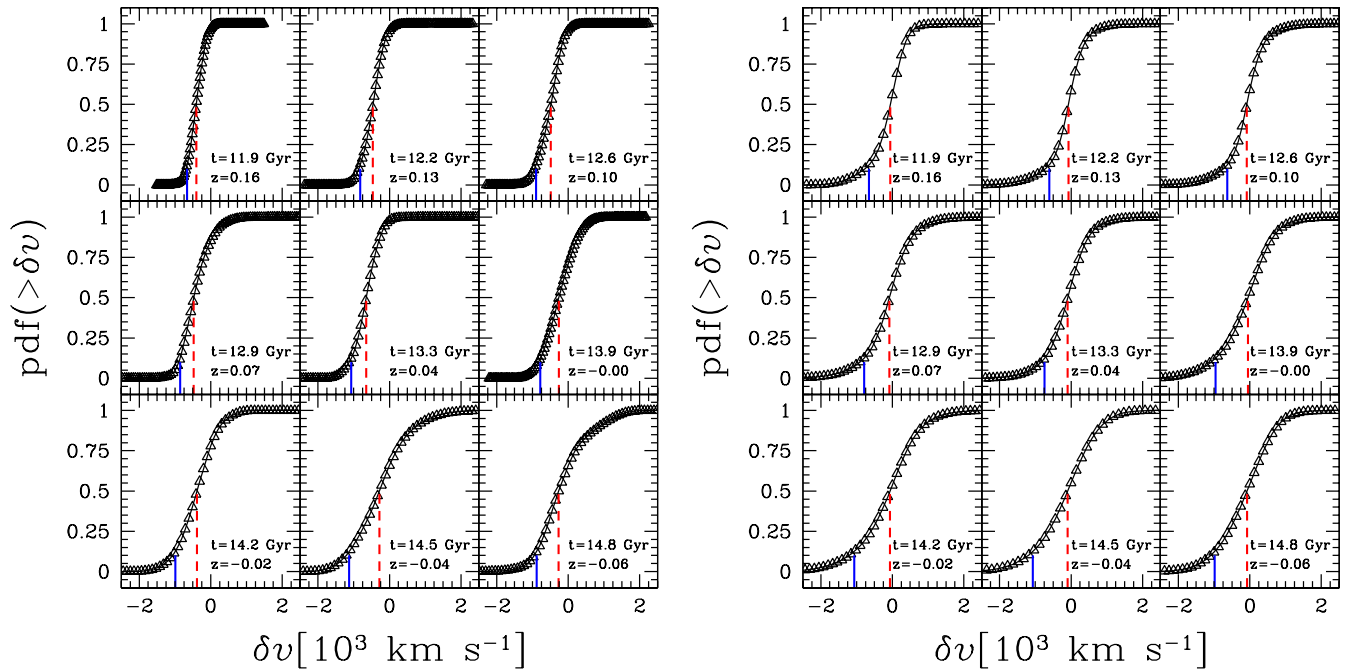


Figure 6. Cumulative probability density function for the compressional (left) and incompressible (right) velocity increment computed at separation given by the injection scale. Time in each panel is the same as in the corresponding panels of Figure 2. The dashed (red) vertical line marks the median value while the solid (blue) vertical line the 12.5th percentile.

of Figure 2, i.e. is around the period of enhanced mass accretion. As for the compressional component we find that it is characterised by a negative median velocity increment, i.e. $\langle \Delta \mathbf{v} \rangle_M < 0$. This implies a systematic convergence of the compressional motions. Such motions can produce heating from adiabatic compression (AdC) of the particles and is important in view of the acceleration mechanisms discussed in the next Section. The heating rate can be approximated as

$$\Gamma_p = \frac{1}{p} \frac{dp}{dt} = -\frac{1}{3} \nabla \cdot \mathbf{v} \approx -\frac{\langle \Delta \mathbf{v} \rangle_M}{3L} \quad (15)$$

We anticipate that while the contribution from this mechanism is comparable to others already proposed in the literature, it is relatively slow and does not change the qualitative picture. Note that no such motions appear in the incompressible velocity component, as expected. Note also how the distribution of the velocity changes with time and in particular broadens in connection with mergers events. However, there is no sign of significant regions of strongly enhanced motions. In fact, the 12.5 percentile value remains typically $\lesssim 10^3$ km s $^{-1}$, comparable to the velocity at the outer scales in Figure 3. This is also of interest from the viewpoint of particle acceleration in the ICM discussed in the next Section.

4. RESULTS (II): STOCHASTIC PARTICLE ACCELERATION

In the following we use the above results concerning the statistical properties of the turbulence to compute the acceleration rates predicted by models based on the interaction of particles with turbulence generated waves. In particular we consider the acceleration processes referred to as non-resonant mechanism (NR; Ptuskin 1988, BL7) and transient-time-damping (TTD; BL7, BL11).

These models have received particular attention in connection with the presence of diffuse radio emission in galaxy clusters. In brief, TTD is a second order Fermi mechanism in which particles in phase-resonance with the fast magneto-sonic waves are reflected through the magnetic mirror effect (Fisk 1976; Miller 1991). In the non-resonant mechanism (Ptuskin 1988), suprathermal particles are accelerated by stochastic fluctuations in the velocity divergence according to the adiabatic process $\frac{dp}{dt} = -\frac{p}{3} \nabla \cdot \mathbf{u}$. Here the correlation scale of the compressional turbulence, ℓ , is much larger than the particle scattering mean-free-path, i.e. $\ell \gg \ell_{mf\dot{p}} \simeq 3D/c$, where D is the diffusion coefficient, assumed homogeneous and isotropic. This process is of the same nature as, and superposes independently to, the adiabatic heating described in Eq. (15). In both the above stochastic models the particles interact with compressional fast magneto-sonic waves, which in the high- β ICM plasma effectively correspond to acoustic waves. The acceleration rates are sensible to a number of assumptions concerning the microphysics of the ICM plasma. In particular the dynamics of the cascade of fast magneto-sonic waves and the resulting cutoff scale. In order to expose how such dependencies emerge in our results, in the following we first briefly review the formulae expressing the acceleration rates that we use below.

The evolution of the distribution function of relativistic particles, f , is described by the transport equation which in the case of isotropic diffusion reads (e.g. Blandford & Eichler 1987)

$$\frac{\partial f}{\partial t} + \mathbf{v} \cdot \nabla f - D_{xx} \nabla^2 f - \frac{1}{p^2} \frac{\partial}{\partial p} \left[p^2 \left(b(p)f + D_{pp} \frac{\partial f}{\partial p} \right) \right] = 0. \quad (16)$$

Here D_{xx} and D_{pp} are the Fokker-Planck diffusion coefficients in configuration and momentum space, respec-

tively and, $b(p) \equiv -dp/dt$, is the particle's total energy loss rate (see e.g., Miniati et al. 2001a). The particle propagation in momentum space can be described as a combination of diffusion governed by the diffusion coefficient, D_{pp} , and advection at the rate

$$\Gamma_p \equiv \frac{\dot{p}}{p} = p^{-3} \frac{\partial}{\partial p} (p^2 D_{pp}) = 4 \frac{D_{pp}}{p^2}. \quad (17)$$

The last equality is based on the fact that for the processes considered below $D_{pp} \propto p^2$. Thus advection in momentum space is linear. This is also the case for adiabatic compression (Eq. 15), which however produces no diffusion. Finally, note that $b(p)$ also acts as a advection term, albeit a nonlinear one. In the following we begin reviewing the expressions for the diffusion coefficients according to the processes of interest.

4.1. Diffusion Coefficients

The diffusion coefficient for the TTD process (BL7 and references therein) can be written, after some manipulation, as

$$D_{pp}(p) = p^2 \frac{\pi I_\theta \left(\frac{c_s}{c}\right)}{8c} \langle k \rangle_W \langle (\delta \mathbf{v}_c)^2 \rangle, \quad (18)$$

where

$$\langle k \rangle_W \equiv \frac{1}{\langle (\delta \mathbf{v}_c)^2 \rangle} \int^{k_c} dk k W(k) \simeq \frac{\zeta_2}{1 - \zeta_2} k_L \left(\frac{k_c}{k_L} \right)^{1 - \zeta_2}. \quad (19)$$

In addition, the total energy is $W(k) \approx 2E(k)$ and is normalised to the velocity dispersion (twice the kinetic energy, see Section 2.2), $k_L \equiv 2\pi/L$, and k_c is the cutoff mode of the spectrum of fast magneto-sonic waves. The integral $I_\theta(x) \equiv \int_0^{\arccos(x)} d\theta \frac{\sin^3 \theta}{|\cos \theta|} \left[1 - \left(\frac{x}{\cos \theta} \right)^2 \right]^2 \approx 5$ for a typical sound speed of 10^8 cm s⁻¹, i.e. $x = c_s/c \simeq 1/300$.

For the non-resonant mechanism Ptuskin (1988), again after some manipulation, we write

$$D_{pp} = p^2 \frac{2}{9} \zeta_2 \frac{\langle (\delta \mathbf{v}_c)^2 \rangle}{D} \left(\frac{k_L D}{c_s} \right)^{\zeta_2} \int_{k_L D/c_s}^{k_c D/c_s} d\xi \frac{\xi^{1 - \zeta_2}}{1 + \xi^2}, \quad (20)$$

where we assume $D = \frac{2\pi}{3} c/k_c$, i.e. we relate the mean free path to the cascade cutoff (BL7). This is a strong simplification and refined assumptions shall be explored in the future. However, as we shall see, as long as $k_c \gg k_L$, this case remains weakly dependent on such fine details. In any case, in general in both cases, the diffusion coefficient depends on the details of the cascade of fast magneto-sonic waves, through the parameters ζ_2 and k_c . Thus in the next Section we summarise how these quantities are determined. Arguably, the other quantities entering the diffusion coefficients, such as the sound speed, c_s (which also determines I_θ), the injection scale L and the corresponding velocity dispersion $\langle (\delta \mathbf{v}_c)^2 \rangle$ can be obtained with reliable approximation from the hydrodynamic simulation.

4.2. Cascade Models

In BL7 the cascade of fast magneto-sonic waves is based on Kraichnan's picture. The cascade rate is determined by the Alfvén speed, $v_A = B/\sqrt{4\pi\rho}$ and is $\tau_A^{-1} = v_A k$, rather than the eddy turnover time, $\tau_{NL}^{-1} = k^{3/2} E(k)^{1/2}$ (Zhou & Matthaeus 1990). Energy transfer to higher modes is therefore faster, resulting in a flatter spectrum, than Kolmogorov's. In particular, given the injection spectrum of turbulent energy per unit mass

$$I(k) = I_0 \delta(k - k_L), \quad I_0 = C_W k_L \frac{\langle (\delta \mathbf{v}_c)^2 \rangle^2}{c_s}, \quad (21)$$

the equilibrium spectrum for the total energy is

$$W(k) \approx 2E(k) = \left(\frac{2C_W}{7} \right)^{\frac{1}{2}} \frac{\langle (\delta \mathbf{v}_c)^2 \rangle}{k_L} \left(\frac{k}{k_L} \right)^{-\frac{3}{2}}. \quad (22)$$

By normalising $k_L W(k_L)$ to the velocity dispersion we infer $C_W = 7/2$ (comparable to $81/14$ in BL7; note, however, that by normalising instead the integral of the total energy one gets $C_W = 7/8$). Kraichnan's scenario, however, should apply when $\tau_A^{-1} \gg \tau_{NL}^{-1}$ (Zhou & Matthaeus 1990), i.e. below the Alfvén scale at $k > k_A = k_L \langle (\delta \mathbf{v}_c)^2 \rangle^{n/2} / v_A^n$, where $n = 3$, respectively 2, for Kolmogorov's and Burgers cases. So it is not clear that this is the dominant mechanism for the cascade of compressional, fast magneto-sonic waves in the high- β ICM. Magneto-sonic waves could partly dissipate through weak shocks. This is indeed what happens in our hydrodynamical model. In this case the equilibrium spectrum is considerably steeper, similar to the case of Burgers' turbulence (Miniati 2014). We will consider this further in our estimates of the acceleration rates below.

Another important quantity entering the estimates of the acceleration rates is the cutoff scale of the turbulent cascade. At this scale the cascade rate equals the dissipation rate, so it depends on both the dissipation mechanism and the cascade model. In BL7 the main damping mechanism of the cascade is TTD of thermal electrons. This assumes that the thermal plasma is collisionless so the long mean-free-path of the thermal particles warrants the resonant interaction with the fast magneto-sonic waves. The azimuthally averaged dissipation rate is

$$\frac{\langle \Gamma_{\text{TTD}} \rangle}{k} \approx \left(\frac{3\pi m_e}{20m_p} \right)^{\frac{1}{2}} c_s \left\langle \frac{\sin^2 \theta}{\cos \theta} e^{-\frac{5m_e}{3m_p \cos^2 \theta}} \right\rangle_\theta, \quad (23)$$

where $\langle \dots \rangle_\theta \sim 2.7$. By equating the Kraichnan's cascade rate and the above dissipation rate leads to (BL7)

$$k_c = \frac{81}{14} \left(\frac{I_0}{c_s} \right) \left[\frac{\langle \Gamma(k) \rangle}{k} \right]^{-2} \approx A k_L \frac{\langle (\delta \mathbf{v}_c)^2 \rangle^2}{c_s^4}, \quad (24)$$

with $A = \left(\frac{270 C_W m_p}{7\pi m_e} \right) \left\langle \frac{\sin^2 \theta}{\cos \theta} e^{-\frac{5m_e}{3m_p \cos^2 \theta}} \right\rangle_\theta^{-2} \approx 11000$, with the above choice of C_W .

If shock dissipation is effective and the cascade is steeper as in Burgers' model, the effective energy transfer rate is slower and the cutoff scale correspondingly larger. One way to roughly estimate the decay rate is to write

$\epsilon_\ell = \langle (\delta \mathbf{v}_c)_\ell^2 \rangle / \tau_\ell = \langle (\delta \mathbf{v}_c)_\ell^3 \rangle / \ell$ so that

$$\tau_\ell^{-1} \approx \frac{\langle (\delta \mathbf{v}_c)_\ell^3 \rangle}{\langle (\delta \mathbf{v}_c)_\ell^2 \rangle} L^{-1} \left(\frac{\ell}{L} \right)^{\zeta_3 - \zeta_2 - 1}. \quad (25)$$

A similar expression can also be found using more rigorous arguments (Landau & Lifshitz 1987). Equating this rate to the TTD rate gives

$$k_c \approx \left(2\pi \frac{\langle \Gamma_{\text{TTD}} \rangle}{k} \frac{\langle (\delta \mathbf{v}_c)_\ell^2 \rangle}{\langle (\delta \mathbf{v}_c)_\ell^3 \rangle} \right)^{-\frac{1}{\zeta_3 - \zeta_2}} k_L \quad (26)$$

which is typically much larger than the value of Eq. (24). Finally, a number of authors have suggested that the effective mean-free-path of the thermal particles could be substantially reduced due to the action of small scale instabilities (Parker 1958; Ginzburg 1979; Schekochihin et al. 2005, 2008). This prevents the resonance of the thermal electrons with the fast magneto-sonic waves suppressing the associated TTD mechanism. This case has been addressed in BL11. The main consequence is that the relativistic particles become the main mechanism for the dissipation of fast magneto-sonic waves through the TTD process. As a result, dissipation of fast magneto-sonic waves becomes less efficient, their cascade extends to much smaller scales and acceleration of relativistic particles becomes much more efficient. Following BL7, we find the azimuthally averaged dissipation rate due to relativistic particles

$$\frac{\langle \Gamma_{CR} \rangle}{k} = \frac{\pi I_\theta q \epsilon_{CR}}{8 \rho c} \quad (27)$$

where $q \simeq 4.5$ is the log-slope of the cosmic-ray distribution function, and ϵ_{CR} is the cosmic-ray energy density. Then the cutoff mode is given by Eq. (24) but with the above dissipation rate, namely

$$k_c \approx \frac{81}{14} C_W \left(\frac{8}{\pi I_\theta q x_{CR}} \right)^2 k_L \frac{\langle (\delta \mathbf{v}_c)_\ell^2 \rangle^2}{c_s^6} c^2, \quad (28)$$

where, $x_{CR} = \epsilon_{CR} / \rho c_s^2$ is the ratio of cosmic-ray to thermal energy. Then the diffusion coefficient for the NR process is given by Eq. (20) with the above value of k_c while the diffusion coefficient associated to the TTD mechanism (Eq. 18) becomes

$$D_{pp} = p^2 C_D \frac{I_0 \xi}{\epsilon_{CR}} = p^2 \frac{C_D C_W \xi}{x_{CR}} k_L \frac{\langle (\delta \mathbf{v}_c)_\ell^2 \rangle^2}{c_s^3}, \quad (29)$$

where $C_D = (2/q)(81/49)^{\frac{1}{2}} \approx 0.57$ with $q \simeq 4.5$. In the above expression we have introduced an additional factor ξ to account for the effectiveness of the above microscales instabilities to render the plasma highly collisional. For example, high temporal or spacial intermittency of the instabilities could still enable some damping of the compressible waves via TTD by thermal particles.

In any case, this scenario boosts significantly the efficiency of the TTD mechanism, while only marginally that of NR. It is worth mentioning that in BL11, Kraichnan's model is assumed for the cascade. As already noted, however, the cascade could partly dissipate also through weak shocks, reducing dramatically the energy in the cascade available for, and the efficiency of, particle acceleration regardless of the plasma collisionality.

In this case the the diffusion coefficient would be given again by Eq. (18) with cutoff scale as in Eq. (26) but with the dissipation rate due to cosmic-rays given in Eq. (27). This results in a larger cutoff mode than the corresponding collisionless case. However, because $\zeta_2 \approx 1$, this larger value has little effect on $\langle k \rangle_W$ (see Eq. 4.1), and hence on D_{pp} , just as in the BL7b case. Therefore we will dismiss this specific case in the following discussion, keeping in mind that it gives similar results to the BL7b case.

4.3. Momentum Advection Rates

Using the statistical properties of the compressional turbulence (Figure 3 and 6) we now compute the advection rates in momentum space (Eq. 17) for the processes discussed in the previous Sections. Remember that, since the diffusion coefficients in these cases turn out proportional to p^2 , the advection timescales are momentum independent. The advection rates are plotted in Figure 7 in units of inverse Gyr, as a function of time in units of Gyr (bottom x-axis), and redshift (top x-axis) for TTD (dotted line), NR (short-dashed line), AdC (long-dashed line), together with their total sum, Tot (solid line and open symbol). The four panels correspond to four different scenarios for the microphysics discussed in the previous Section. In particular, the top-left panel corresponds to the BL7 case, meaning that the cascade of compressional modes is based on Kraichnan's model with cutoff given by Eq. (24). The case of the top-right panel (BL7k) is the same as BL7 except for the cascade's slope, which is taken from the hydrodynamic model. Of course this is not self-consistent but provides a useful intermediate step to the results of the bottom left panel (BL7b) where the full cascade is based on the hydrodynamical model with cutoff given by Eq. (26). Finally, the bottom right panel assumes the scenario in BL11, namely Kraichnan's cascade model with cutoff given by Eq. (28) motivate by an effective high collisionality of the ICM plasma. The acceleration rates are compared to the minimum energy loss rate, Γ_{\min} , suffered by a relativistic electron emitting synchrotron radiation at the following frequencies: 300 MHz (lower dot-dashed cyan curve), 1.4 GHz (middle) and 8 GHz (upper). These are the typical frequencies at which diffuse radio emission from the ICM is observed. At a given frequency, ν , and redshift, the minimum energy loss rate is

$$\Gamma_{\min}(\nu) = a (1+z)^{\frac{7}{2}} \left(\frac{\nu}{\nu_{\text{CMB}}} \right)^{\frac{1}{2}} \text{Gyr}^{-1}, \quad (30)$$

occurring in a magnetic field strength

$$B_{\min} = \frac{B_{\text{CMB}}(z)}{\sqrt{3}} = \frac{B_{\text{CMB}}(0)}{\sqrt{3}} (1+z)^2, \quad (31)$$

where $a = 6.2 \times 10^{-4}$, $\nu_{\text{CMB}} = e B_{\text{CMB}} / (2\pi m_e c) \approx 9\text{Hz}$ and B_{CMB} is the CMB energy density expressed in terms of magnetic field strength. Also, the momentum of the radiating particles is

$$p_{\min} = (1+z)^{-\frac{1}{2}} \left(\frac{\nu}{\nu_{\text{CMB}}} \right)^{\frac{1}{2}} m_e c. \quad (32)$$

For reference in Figure 7 we also show the minimum energy losses suffered by a suprathermal particle in an ICM

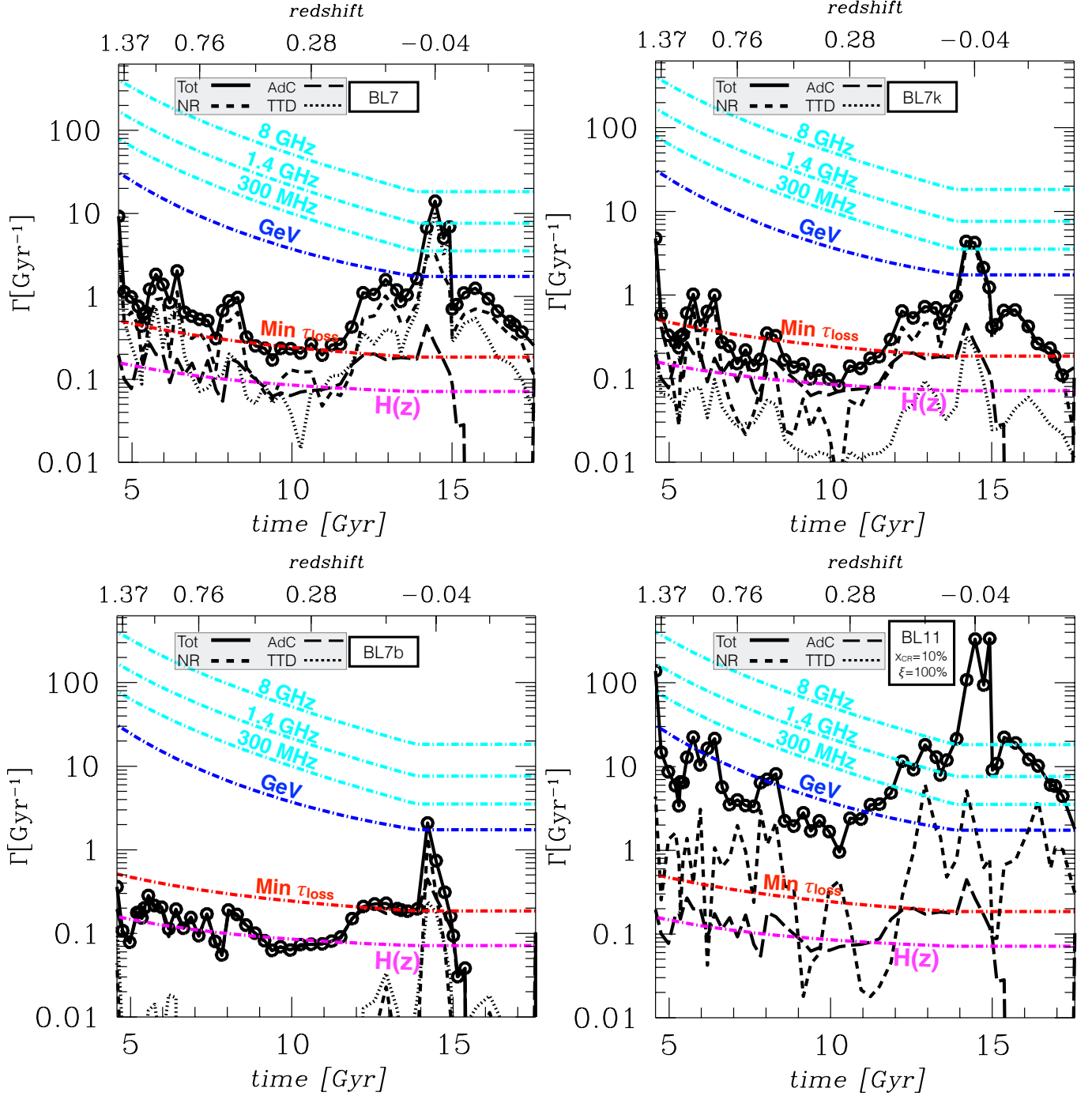


Figure 7. Acceleration rates due to the NR (short-dash), TTD (dotted) mechanisms and AdC (long dash) as a function of time in units of Gyr (bottom axis) or redshift (top axis). The four panels correspond to the different physical scenarios for the microphysics of BL7 (top left), BL7k (top right), BL7b (bottom left), BL11 with $x_{CR} = 10\%$ and $\xi = 100\%$ (bottom right) and their total sum (solid line with open dot symbols). The cyan curves correspond to the minimum energy loss rate of an electron emitting synchrotron radiation at 300 MHz (lower), 1.4 GHz (middle) and 8 GHz (upper). Also shown are the minimum energy losses suffered by a suprathermal particle in the ICM for a number density of free electrons 10^{-3} cm^{-3} and magnetic field strength of 10^{-6} G (red curve); the energy loss rate for a GeV electron (blue curve); and the Hubble rate (magenta).

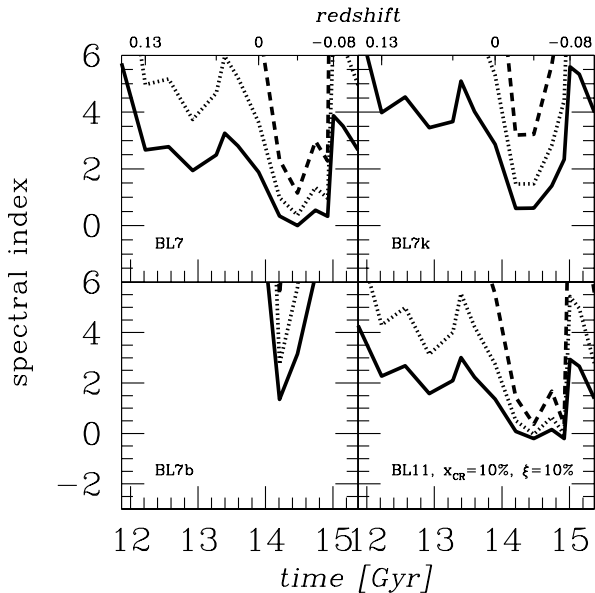


Figure 8. Spectral index for emission at 300 MHz (solid line), 1.4 GHz (dotted line) and 8 GHz (dashed line) as a function of time in Gyr (bottom axis) and redshift (top axis). The top left panel is for BL7, the top right for BL7k and the bottom left for BL7b (same as the corresponding top panels in Figure 7). The bottom right panel is for BL11 with $x_{CR} = 10\%$ and an additional intermittency factor, $\xi = 10\%$.

with number density of free electrons $n_e = 10^{-3} \text{ cm}^{-3}$ and magnetic field strength $B = 10^{-6} \text{ G}$ (red curve), the energy loss rate for a GeV electron (blue curve), and the Hubble rate (magenta).

In the BL7 scenario (top-left panel) the total advection rate is basically always above the minimum loss rate curve, meaning that it is sufficient to maintain the bulk of a low energy (ca 100 million eV) but suprathermal population of electrons. In this scenario the AdC process contributes comparably to TTD and NR up to 12 Gyr, is almost negligible during the merger event and actually contributes to the cooling of the particles after core passage. Note that the NR advection rate increases significantly during the 3 Gyr long period of high mass accretion rate described in Section 3.1 while the TTD only during the major merger itself. In addition, the two peaks in the total acceleration rate correspond to core passage of the minor and major merger events. During the major merger in particular, in this scenario the total advection rate reaches values close to the minimum energy losses of a 1.4 GHz emitting electron. When the slope of the cascade is modified from Kraichnan to the value of the hydrodynamic model (top-left) the TTD rate drops dramatically, while the NR rate is almost unaffected. The drop of TTD rate is ascribed to the sensitive dependence of the quantity $\langle k \rangle_W$ on ζ_2 in Eq. (19). In particular, $\langle k \rangle_W$ and, as a consequence, D_{pp} , become progressively smaller for ζ_2 progressively larger than $\frac{1}{2}$, which is what happens when Kraichnan's slope is replaced by the one from the hydrodynamic model. Note that this effect occurs regardless of the plasma collisionality, i.e. TTD is generally suppressed when $\zeta_2 \rightarrow 1$. On the other hand, the NR rate is less sensitive to changes in ζ_2 and, as long as $k_c \gg k_L$, it becomes almost independent of k_c as $\zeta_2 \rightarrow 1$. However, if one assumes a pure hydrodynamic

cascade in which the fast magneto-sonic modes are dissipated at weak shocks, the cascade cutoff scale becomes very large and both TTD and NR mechanisms become very inefficient. This is illustrated in the bottom left panel of Figure 7, where the total advection rate is now completely dominated by AdC falls below the minimum loss rate except during the major merger event. Finally, in the BL11 scenario (bottom right panel) the TTD advection rate is highly boosted by the effective collisionality of the thermal plasma, which suppresses the damping of the fast magneto-sonic waves responsible for the acceleration of the particles. The plots assume a cosmic-ray energy fraction $x_{CR} = 10\%$, no intermittency, $\xi = 100\%$, as well as Kraichnan's cascade model. The NR mechanism is much less affected for the same reasons as above, and its rates comparable to those in the BL7 scenario. Obviously AdC is not affected, as in the previous panels. As already mentioned, when $\zeta_2 \rightarrow 1$ TTD mechanism is suppressed even in the case of high plasma collisionality.

We now turn to the properties of the emitted radiation in the various scenarios. While the time evolution of the emitting particles could be integrated in time using a numerical scheme (see e.g. Miniati 2001, 2007), here we adopt a simplified and more straightforward analytic method, leaving the more accurate treatment for the future. In particular we are interested in the evolution of the spectral index of the synchrotron radiation of the emitting particles

$$\alpha \equiv -\frac{\partial \log j_{syn}(\nu)}{\partial \log \nu}. \quad (33)$$

We assume conditions of approximate steady-state equilibrium. This applies for example when, during a merger event, the rise of turbulent energy is about to turn around and the distribution function time derivative to change sign. We also consider the multi-GeV energy range, where particle cooling rate, Γ_{syn+IC} , is dominated by synchrotron and inverse Compton mechanism (Rybicki & Lightman 1979). Under these conditions the equilibrium particle distribution function is simply

$$f(p) = f_0 e^{-q}, \quad q \approx \frac{4\Gamma_{syn+IC}}{\Gamma_p}, \quad (34)$$

and the synchrotron spectrum

$$j_{syn}(\nu) \propto \left(\frac{2\nu}{3\nu_B}\right)^{\frac{3}{2}} \int dx \frac{F(x)}{x^{\frac{5}{2}}} \int d\mu \frac{e^{-q(x,\mu)}}{(1-\mu^2)^{\frac{1}{4}}}, \quad (35)$$

where $F(x) = x \int_x^\infty K_{5/3}(z) dz$, $K_{5/3}$ is the modified Bessel's function of order $5/3$ and μ is the particles pitch angle, assumed uniformly distributed. The magnetic field entering the cyclotron frequency is chosen to be B_{CMB} so that $\nu_B = \nu_{CMB}$, corresponding to the most favourable conditions for synchrotron emission (see above). It is then easy to carry out the log-derivative of the emissivity in Eq. (35) to find out the time-dependent spectral index defined in Eq. (33) characterising the various scenarios discussed above in connection with Figure 7. This involves some integration which is straightforwardly carried out numerically.

Note that when $\Gamma_p < \Gamma_{syn+IC}$, the particles are not advected towards higher values in momentum space but can still be accelerated diffusively (Brunetti & Lazarian

2011). This is in fact what produces the exponential roll-off in the distribution function of Eq. 34. And it is these particles in the exponential tail that are thought to produce the steepening spectrum characteristic of the diffuse radio emission observed in galaxy clusters.

The results are presented in Figure 8, for emission at 300 MHz (solid line), 1.4 GHz (dotted line) and 8 GHz (dashed line). The top two panels and the bottom left panel correspond, respectively, to the BL7, BL7k and BL7b scenarios (as the corresponding panels of Figure 7), while the bottom panel is for the BL11 scenario assuming $x_{CR} = 10\%$ and $\xi = 10\%$ (vs $x_{CR} = 10\%$ and $\xi = 100\%$ in Figure 7). The time span is restricted to the few Gyr around the time of high mass accretion rate. The plots show that in general the time dependence of the spectral index is, as expected from the previous figure, flattening and steepening before and after core passage, respectively, with the minimum value corresponding to the peak of the advection rate during the major merger. In the BL7 case the spectral index at 300 MHz is between 0 and 1.5 for about a Gyr, between 0.2 and 2 for almost a Gyr at 1.4GHz, and between 2 and 4 at 8GHz. These values are reasonable for classical radio halos with spectral index around 1 (Ferrari et al. 2008; Feretti et al. 2012). Steeper spectral indexes are predicted in the slightly less efficient cases of BL7k, where $\alpha > 0.5 - 2$ and $> 1.5 - 4$, at 300 MHz, 1.4 GHz, respectively, only partially viable for classical radio halos but suitable for the ultra-steep halos ($\alpha \gtrsim 2$, Cassano et al. 2010a; Brunetti et al. 2008; Cassano et al. 2013), while in the inefficient BL7b case the spectral index is very large and basically inconsistent with the observations. Note that according to Eq. (30) the energy losses grow quite rapidly with redshift, as $(1+z)^{\frac{7}{2}}$. So the situation may become also challenging for the BL7 scenario at higher redshifts, namely $z \simeq 0.4 - -0.5$. However, this topic deserved a separate and more focused discussion and investigation, based on the specific characteristics of halos at those redshifts. In the case of BL11 the advection rates are much higher, so one expects lower spectral indexes. This is indeed the case. When $x_{CR} = 10\%$ and $\xi = 100\%$, corresponding to the bottom-right panel of Figure 7 we obtain results inconsistent with observations. We therefore consider the case $x_{CR} = 10\%$ and $\xi = 10\%$. For these parameters the spectra during the major merger are still rather flat. At low frequencies they remain within the observed range even prior the major merging, i.e. during the phase of enhanced mass accretion including the (triple) minor merger, so the sources acquire a long lifetime of almost 3 Gyr (the lifetime being roughly defined as the time interval during which the spectral index remains consistent with observed values).

5. DISCUSSION

The analysis in the preceding Section indicates that the acceleration rate due to stochastic acceleration processes increase significantly during the episode of high mass accretion rate, peaking in value during the major merger event. This is in general, qualitative agreement with requirements from astronomical observations, indicating that sources of diffuse radio emission in GC occur in connection with energetic mergers. Important details related to the microphysics of the ICM remain to be understood, however, as they affect significantly the quanti-

tative predictions of the model. We discuss these briefly in the following.

In the BL7 scenario, which assumes Kraichnan's cascade for fast magnetosonic waves, the acceleration rate appears sufficient to power synchrotron spectra with consistent with classical radio halos. When the assumption of Kraichnan's model are relaxed towards the steeper cascade model produced by the simulation and based on partial dissipation by weak shocks, the situation worsens noticeably. In this case it becomes difficult to reconcile the results with observations. Thus the nature of the cascade of fast magneto sonic waves in the ICM has a fundamental impact on the acceleration efficiency of both TTD and NR mechanisms. It would therefore be very valuable to understand to what extent Kraichnan's scenario applies and to what extent dissipation by weak shocks steepens the cascade. Finally, in the plain version of the BL11 scenario, the acceleration efficiency become potentially too high. Here the turbulence is mainly dissipated via TTD by cosmic-ray protons in the ICM and the diffusion coefficients is inversely proportional to their energy density (see Eq. 29). This quantity has been constrained by several gamma-ray experiments to $x_{CR} \leq 1\%$ (Ackermann et al. 2014; Huber et al. 2013; Aleksić et al. 2012). In our estimate we have relaxed this upper limit to 10% (assuming, e.g., the cosmic-ray spatial distribution is broader than the thermal gas, Miniati et al. 2001b). Of course in this case, secondary e^+e^- generated in hadronic collisions by the above cosmic-ray protons might also produce significant radio emission in the magnetic field given by Eq. (31) (e.g. Miniati 2003). In addition we have assumed a reduced effect of micro-instabilities on the plasma collisionality such that $\xi \approx 10\%$. In this case we obtain spectra that perhaps remains too flat, but in a reasonable range, and a source lifetime roughly consistent with observations. Of course the above parameters such as x_{CR} and ξ ideally should be determined independently and *not* chosen to reproduce the observations. In any case, the microphysics apparently plays a crucial role here. The important implications of cosmic-ray feedback was also discussed by Beresnyak et al. (2013); Brunetti & Jones (2014). It is important to remember that we have so far considered a specific magnetic field, B_{min} (see Eq. 31). Without entering a full discussion on this quite complex topic, we should at least mention that larger ICM magnetic fields than B_{min} are likely and would favour the collisional scenario.

It is worth noting that while the radiative losses at fixed frequency increase rapidly with redshift (see Eq. 30), RH are observed up to $z = 0.5$, with a constant number of sources per redshift interval out to $z = 0.3$. These objects are typically more massive than the object in our simulation, so their turbulent motions and predicted acceleration rates will be correspondingly higher. But if we extrapolate our simulated cluster ($M < 2 \times 10^{15} M_{\odot}$) at these modest z we find the acceleration rates in the BL7 scenario perhaps insufficient for RHs. Thus a discovery of a population Coma-like RHs at these and higher redshift will rule out purely collision less flavour of compressional turbulence acceleration in the ICM. This might soon be checked by surveys with LOFAR and more in the future with SKA. It is worth reminding that the major merger experienced by the simulated GC is a rarely strong one (Section 3.1), with a

relative velocity occurring in only 5% of the cases. Thus the acceleration rates are not limited by of a particularly weak merger.

In addition, the pdf-statistics of the increments of compressional velocity in Figure 4 shows that very high velocity increments above 10^3 km s^{-1} occupy less than 10% of the volume. Sufficiently strong acceleration might occur in a sub-volume in which the turbulence is particularly strong. However, in order for this sub-volume would to have covering factor of order unity, the emitting regions would have to be rather thin (for example, for a 10% subvolume implied by the above statistics, arranged to cover a surface of diameter 1 Mpc, one infer a thickness less than 0.1 Mpc). This might lead to polarised emission, a possibility which should be investigated in more details in the future.

Finally, from the results in the previous section it is clear that sufficient compressional turbulence is generated only close to core passage of the major merger event. The origin of the classical, moderately steep radio halo of the Coma cluster, therefore, remains a puzzle in the less efficient scenarios, given that this cluster experienced his the last major merger about 2 Gyr ago (Burns et al. 1994). In addition, while BL11 case with small x_{CR} and large ξ is sufficiently efficient to produce diffuse radio emission even during minor merger events, such as the one possibly currently experienced by Coma cluster, it is essential to understand how those parameters change with changing turbulent conditions in the plasma (constant values would be inconsistent with observations).

So, perhaps the most important conclusion emerging from the above discussion is that RH are complex phenomena in which a hierarchy of processes are at work. Unlike other cases in astrophysics the subtleties of the ICM plasma microphysics here appear to play an important role with a potentially strong impact. The study of RH therefore offers a unique opportunity to learn about these processes. In this context the ability to model reliably the ICM turbulence with high resolution simulations is instrumental because it removes an important unknown of the problem, namely the turbulence statistics, and allows to start addressing these more elusive processes that characterise the acceleration physics. Obviously, while in this paper we have used the properties of a single GC, it will be important to improve on the analysis, extend it to a representative sample of simulated GC and explore the fully MHD case, amongst others. Eventually, these efforts might be corroborated by measurements of the ICM turbulence thanks to the advent of high precision X-ray spectrometers such as Astro-H¹ and Athena², which will have energy resolution of a few eV, and perhaps the help of innovative analysis techniques (Schuecker et al. 2004; Churazov et al. 2004; Sanders et al. 2011; Zhuravleva et al. 2012; Gaspari & Churazov 2013; Zhuravleva et al. 2014; Gaspari et al. 2014).

Another important point to constrain the physical scenario is to continue verifying the connection between the compressional turbulence driving the stochastic acceleration of the supra-thermal particles, and the RH properties (e.g. Cassano et al. 2010b; Russell et al. 2011; Basu

2012, 2013; Cassano et al. 2013). This can be achieved by looking at other testable implications emerging from this model. There are two such potential tests. Although they might prove not straightforward, they may become feasible with future surveys. First, we note that in Figure 7 the peaks in the total acceleration rate correspond to core passage during the two mergers events, while the roughly linear rise and fall around the peaks is correlated with the nearing and departing of the merging structures. This is of course due to gas compression and decompression following the passage of the substructure through the main cluster. Thus strong compressional turbulence persists during $\tau_c \approx 2d/v_{rel}$, where $d \approx L \approx R_{vir}/3$ is the distance at which turbulence injection begins, and $v_{rel} \approx a_v v_{vir}$, the relative velocity of the merging structures with $a_v \gtrsim 1$, and R_{vir} and v_{vir} , the virial radius and velocity respectively. Thus the simulation also predicts a correlation of radio power with distance of the merging cores. In addition, as discussed in Section 4.3 and shown in Figure 8, the spectral index is time dependent and should get flatter with the approaching of the merging cores, and steeper with the departing of the same. Thus, like the radiation power, the spectral index should show some correlation with distance of the merging cores. Based on the level of compressional turbulence alone, these correlations should be symmetric with respect to time since core passage. Actually in both cases there will be a 'space-lag' corresponding to the distance traveled by the merging cores during a cooling time, i.e. $d_{lag} \sim v_{rel} \Gamma_p^{-1}$. In addition, more subtle complications may arise depending on the detail of the acting microphysics. In any case some correlation should emerge above the noise, particularly for strong merger events, provided a sufficiently large number of RH sources becomes available. While the statistical details are important, they are not attempted here as beyond the scope of the paper.

6. SUMMARY AND CONCLUSIONS

In this paper we have used results from the Matryoshka run (Miniati 2014) to model the time dependent statistical properties of the turbulence in the ICM of a massive GC. The very high resolution of the simulation across the virial volume allows us to model the cascade of hydrodynamic turbulence and capture reliably its inertial range and outer scale. We have also decomposed the velocity field into compressional and incompressible components and measured for each case the longitudinal and transverse structure functions, particularly those of second order which are of interest in this study. We have looked at the history of turbulent energy and its fraction in compressional motions, and made a connection to the mass accretion history of the GC. One interesting point is that at late time, $z \approx 0$ the GC experiences a major merger, raising significantly the level turbulent energy and the compressional fraction thereof. However, the mass accretion rate and, consequently, the turbulent energy increase significantly for an extended period of time which is longer than the duration of the merger. We have ascribed this to the fact that spatial clustering of mass gives rise to a temporal clustering of mass accretion (Peebles 1993). We have also looked at other statistical properties of the turbulence, in particular the ratio of the second order transverse and longitudinal structure

¹ <http://astro-h.isas.jaxa.jp>

² <http://sci.esa.int/ixo>

functions. This reveals that the conditions of the flow are often approximately consistent with fully developed turbulence, as departures following merger events settle in about an eddy turnover time. In terms of velocity statistics we have considered the pdf of the velocity increments at the injection scale. We have found that while the median value is negligible for the incompressible component, it is negative for the compressional velocity, indicating a systematic convergence of weak shocks and adiabatic heating of the particles scattering off them.

We have extracted the relevant turbulence properties to estimate the particle acceleration rates due to stochastic processes, and compared their predictions with observations of diffuse radio emission in GC. In particular, we have considered the TTD (Fisk 1976; Miller 1991) and NR (Ptuskin 1988) mechanism, considered in connection with the origin of RH phenomena in BL7 and BL11. These mechanisms are based on the interactions of the particles with compressional waves which, in the high- β ICM plasma, are represented primarily by fast magneto-sonic waves. The acceleration rates depend on both the amount of turbulent energy but also on detailed aspects of the physics of the ICM plasma determining the cascade of the compressional waves. These aspects are not captured by the simulation. However, a dependable numerical models such as this, removes from the problem the unknown represented by the hydrodynamical turbulence, allowing the investigation of assumptions concerning micro-physics of the ICM plasma. The results reported in this paper indicate that the microphysics of the ICM plasma affects significantly the efficiency of the above stochastic acceleration processes. Particularly important are the details of the cascade of fast magneto-sonic waves affected by the plasma collisionality of the thermal ICM and the effectiveness of dissipation processes such as weak shocks. The TTD mechanism can become very efficient, even during minor mergers, but this requires understanding of how plasma microscopic behaviour changes during the such mergers, as the predictions become otherwise inconsistent with observations. We have proposed two new tests to collect additional evidence for the role of stochastic processes in RH (e.g. Cassano et al. 2010b; Russell et al. 2011; Basu 2012, 2013; Cassano et al. 2013) based on the rapid rise and fall of the population of emitting relativistic particles, following the rise and fall of the turbulence. The tests basically concern a statistical correlation of the radio power and the spectral index with distance of the merging cores. Given the statistical nature of these tests, large catalogues of RH are probably necessary which could become available with new surveys by powerful instruments such as LOFAR and SKA.

The author gratefully acknowledges several useful discussions with G. Brunetti, not least during a visit at the hospitable Istituto di Radio Astronomia. This work was supported by a grant from the Swiss National Supercomputing Center (CSCS) under project ID S275 and S419.

REFERENCES

- Ackermann, M., Ajello, M., Albert, A., et al. 2014, *The Astrophysical Journal*, 787, 18
- Aleksić, J., Alvarez, E. A., Antonelli, L. A., et al. 2012, *Astronomy and Astrophysics*, 541, 99
- Basu, K. 2012, *Monthly Notices of the Royal Astronomical Society: Letters*, 421, L112
- . 2013, *Astronomische Nachrichten*, 334, 350
- Benson, A. J. 2005, *Monthly Notices of the Royal Astronomical Society*, 358, 551
- Beresnyak, A. 2012, *Monthly Notices of the Royal Astronomical Society*, 422, 3495
- Beresnyak, A., Xu, H., Li, H., & Schlickeiser, R. 2013, *The Astrophysical Journal*, 771, 131
- Bertschinger, E. 2001, *ApJS*, 137, 1
- Biffi, V., Dolag, K., & Böhringer, H. 2011, *MNRAS*, 413, 573
- Blandford, R., & Eichler, D. 1987, 154, 1
- Blasi, P., & Colafrancesco, S. 1999, *Astroparticle Physics*, 12, 169
- Bodo, G., Cattaneo, F., Ferrari, A., Mignone, A., & Rossi, P. 2011, *ApJ*, 739, 82
- Brunetti, G., & Jones, T. W. 2014, *International Journal of Modern Physics D*, 23, 30007
- Brunetti, G., & Lazarian, A. 2007, *Monthly Notices of the Royal Astronomical Society*, 378, 245
- . 2011, *Monthly Notices of the Royal Astronomical Society*, 410, 127
- Brunetti, G., Setti, G., Feretti, L., & Giovannini, G. 2001, *Monthly Notices of the Royal Astronomical Society*, 320, 365
- Brunetti, G., Giacintucci, S., Cassano, R., et al. 2008, *Nature*, 455, 944
- Buote, D. A. 2001, *The Astrophysical Journal*, 553, L15
- Burns, J. O., Roettiger, K., Ledlow, M., & Klypin, A. 1994, 427, L87
- Cassano, R., Brunetti, G., Röttgering, H. J. A., & Brügggen, M. 2010a, *Astronomy and Astrophysics*, 509, 68
- Cassano, R., Etori, S., Giacintucci, S., et al. 2010b, *The Astrophysical Journal Letters*, 721, L82
- Cassano, R., Etori, S., Brunetti, G., et al. 2013, *The Astrophysical Journal*, 777, 141
- Cho, J., Vishniac, E. T., Beresnyak, A., Lazarian, A., & Ryu, D. 2009, *The Astrophysical Journal*, 693, 1449
- Churazov, E., Forman, W., Jones, C., Sunyaev, R., & Böhringer, H. 2004, *Monthly Notices of the Royal Astronomical Society*, 347, 29
- Clarke, T. E., & Enßlin, T. A. 2006, *The Astronomical Journal*, 131, 2900
- Colella, P. 1990, *Journal of Computational Physics (ISSN 0021-9991)*, 87, 171
- de Kármán, T., & Howarth, L. 1938, *Proceedings of the Royal Society of London. Series A, Mathematical and Physical Sciences*, 164, 192
- Dolag, K., Vazza, F., Brunetti, G., & Tormen, G. 2005, *MNRAS*, 364, 753
- Donnert, J., & Brunetti, G. 2014, *Monthly Notices of the Royal Astronomical Society*, 443, 3564
- Donnert, J., Dolag, K., Brunetti, G., & Cassano, R. 2013, *Monthly Notices of the Royal Astronomical Society*, 429, 3564
- Eisenstein, D. J., & Hu, W. 1998, *ApJ*, 496, 605
- Eisenstein, D. J., & Hut, P. 1998, *The Astrophysical Journal*, 498, 137
- Enßlin, T., Pfrommer, C., Miniati, F., & Subramanian, K. 2011, *Astronomy and Astrophysics*, 527, 99
- Faltenbacher, A., Kravtsov, A. V., Nagai, D., & Gottlöber, S. 2005, *MNRAS*, 358, 139
- Feretti, L., Giovannini, G., Govoni, F., & Murgia, M. 2012, *The Astronomy and Astrophysics Review*, 20, 54
- Ferrari, C., Govoni, F., Schindler, S., Bykov, A. M., & Rephaeli, Y. 2008, *Space Science Reviews*, 134, 93
- Ferrari, C., Maurogordato, S., Cappi, A., & Benoist, C. 2003, *Astronomy and Astrophysics*, 399, 813
- Fisk, L. A. 1976, *Journal of Geophysical Research*, 81, 4633
- Gaspari, M., & Churazov, E. 2013, *Astronomy and Astrophysics*, 559, 78
- Gaspari, M., Churazov, E., Nagai, D., Lau, E. T., & Zhuravleva, I. 2014, *Astronomy and Astrophysics*, 569, A67
- Ginzburg, V. L. 1979, *Theoretical Physics and Astrophysics, International Series in Natural Philosophy (Oxford: Pergamon)*
- Hallman, E. J., & Jeltama, T. E. 2011, *MNRAS*, 418, 2467

- Huber, B., Tchernin, C., Eckert, D., et al. 2013, *Astronomy and Astrophysics*, 560, 64
- Iapichino, L., & Niemeyer, J. C. 2008, *MNRAS*, 388, 1089
- Jaffe, W. J. 1977, *Astrophysical Journal*, 212, 1
- Keshet, U., & Loeb, A. 2010, *The Astrophysical Journal*, 722, 737
- Komatsu, E., Dunkley, J., Nolta, M. R., et al. 2009, *ApJS*, 180, 330
- Landau, L. D., & Lifshitz, E. M. 1987, *Course of Theoretical Physics*, Vol. 6, *Fluid Mechanics*, 2nd edn. (Oxford: Pergamon Press)
- Lau, E. T., Kravtsov, A. V., & Nagai, D. 2009, *ApJ*, 705, 1129
- Lee, J., & Komatsu, E. 2010, *The Astrophysical Journal*, 718, 60
- Miller, J. A. 1991, 376, 342
- Miniati, F. 2001, *Computer Physics Communications*, 141, 17
- . 2003, *Monthly Notice of the Royal Astronomical Society*, 342, 1009
- . 2007, *Journal of Computational Physics*, 227, 776
- . 2014, *The Astrophysical Journal*, 782, 21
- Miniati, F., & Colella, P. 2007, *Journal of Computational Physics*, 227, 400
- Miniati, F., Jones, T. W., Kang, H., & Ryu, D. 2001a, *The Astrophysical Journal*, 562, 233
- Miniati, F., & Martin, D. F. 2011, *The Astrophysical Journal Supplement*, 195, 5
- Miniati, F., Ryu, D., Kang, H., & Jones, T. W. 2001b, *The Astrophysical Journal*, 559, 59
- Miniati, F., Ryu, D., Kang, H., et al. 2000, *The Astrophysical Journal*, 542, 608
- Nagai, D., Vikhlinin, A., & Kravtsov, A. V. 2007, *ApJ*, 655, 98
- Parker, E. N. 1958, *Physical Review*, 109, 1874
- Parkin, E. R., & Bicknell, G. V. 2013, *MNRAS*, arXiv:1306.1084
- Paul, S., Iapichino, L., Miniati, F., Bagchi, J., & Mannheim, K. 2011, *The Astrophysical Journal*, 726, 17
- Peebles, P. J. E. 1993, *Principles of Physical Cosmology* (Princeton New Jersey: Princeton University Press)
- Petrosian, V. 2001, *The Astrophysical Journal*, 557, 560
- Pfrommer, C., Enßlin, T. A., & Springel, V. 2008, *Monthly Notices of the Royal Astronomical Society*, 385, 1211
- Porter, D. H., & Woodward, P. R. 2000, *ApJS*, 127, 159
- Ptuskin, V. S. 1988, *Soviet Astronomy Letters*, 14, 255
- Russell, H. R., van Weeren, R. J., Edge, A. C., et al. 2011, *Monthly Notices of the Royal Astronomical Society: Letters*, 417, L1
- Rybicki, G. B., & Lightman, A. P. 1979, *Radiative Processes in Astrophysics* (New York: John Wiley and Sons)
- Ryu, D., Kang, H., Cho, J., & Das, S. 2008, *Science*, 320, 909
- Sanders, J. S., Fabian, A. C., & Smith, R. K. 2011, *Monthly Notices of the Royal Astronomical Society*, 410, 1797
- Sarkar, S., Erlebacher, G., Hussaini, M. Y., & Kreiss, H. O. 1991, *Journal of Fluid Mechanics* (ISSN 0022-1120), 227, 473
- Schekochihin, A. A., Cowley, S. C., Kulsrud, R. M., Hammett, G. W., & Sharma, P. 2005, *ApJ*, 629, 139
- Schekochihin, A. A., Cowley, S. C., Kulsrud, R. M., Rosin, M. S., & Heinemann, T. 2008, *Physical Review Letters*, 100, 081301
- Schlickeiser, R., Sievers, A., & Thiemann, H. 1987, *Astronomy and Astrophysics* (ISSN 0004-6361), 182, 21
- Schuecker, P., Finoguenov, A., Miniati, F., Böhringer, H., & Briel, U. G. 2004, *Astronomy and Astrophysics*, 426, 387
- Subramanian, K., Shukurov, A., & Haugen, N. E. L. 2006, *Monthly Notices of the Royal Astronomical Society*, 366, 1437
- Valdarnini, R. 2011, *A&A*, 526, A158
- Vazza, F., Brunetti, G., Gheller, C., Brunino, R., & Brüggén, M. 2011, *Astronomy and Astrophysics*, 529, 17
- Vazza, F., Brunetti, G., Kritsuk, A., et al. 2009, *Astronomy and Astrophysics*, 504, 33
- Viallet, M., Meakin, C., Arnett, D., & Mocák, M. 2013, *ApJ*, 769, 1
- Wetzel, A. R. 2011, *Monthly Notices of the Royal Astronomical Society*, 412, 49
- Zhou, Y., & Matthes, W. H. 1990, *Journal of Geophysical Research*, 95, 14881
- Zhuravleva, I., Churazov, E., Kravtsov, A., & Sunyaev, R. 2012, *Monthly Notices of the Royal Astronomical Society*, 422, 2712
- Zhuravleva, I., Churazov, E. M., Schekochihin, A. A., et al. 2014, *The Astrophysical Journal Letters*, 788, L13
- ZuHone, J. A., Markevitch, M., Brunetti, G., & Giacintucci, S. 2013, *The Astrophysical Journal*, 762, 78